

Detection of strong scattering close to the eclipse region of PSR B1957+20

J. T. Bai¹, S. Dai^{2*}, Q. J. Zhi^{1†}, W. A. Coles³, D. Li^{4,5,6}, W. W. Zhu^{4,5}, G. Hobbs⁷, G. J. Qiao⁸, N. Wang⁹, J. P. Yuan⁹, M. D. Filipovic², J. B. Wang⁹, Z. C. Pan^{4,5}, L. H. Shang¹, S. J. Dang¹, S. Q. Wang⁹, C. C. Miao^{4,5}

¹*School of Physics and Electronic Science, Guizhou Normal University, Guiyang, 550001, People's Republic of China*

²*School of Science, Western Sydney University, Locked Bag 1797, Penrith South DC, NSW 2751, Australia*

³*Department of Electrical and Computer Engineering, University of California, San Diego, La Jolla, CA 92093, USA*

⁴*National Astronomical Observatories, Chinese Academy of Sciences, Beijing 100101, People's Republic of China*

⁵*University of Chinese Academy of Sciences, Beijing 100049, People's Republic of China*

⁶*NAOC-UKZN Computational Astrophysics Centre, University of KwaZulu-Natal, Durban 4000, South Africa*

⁷*CSIRO Space and Astronomy, PO Box 76, Epping, NSW 1710, Australia*

⁸*School of Physics, Peking University, Beijing 100871, People's Republic of China.*

⁹*Xinjiang Astronomical Observatory, 150, Science-1 Street, Urumqi, 830011 Xinjiang, People's Republic of China*

Accepted XXX. Received YYY; in original form ZZZ

ABSTRACT

We present the first measurement of pulse scattering close to the eclipse region of PSR B1957+20, which is in a compact binary system with a low-mass star. We measured pulse scattering time-scales up to 0.2 ms close to the eclipse and showed that it scales with the dispersion measure (DM) excess roughly as $\tau \propto \Delta\text{DM}^2$. Our observations provide the first evidence of strong scattering due to multi-path propagation effects in the eclipsing material. We show that Kolmogorov turbulence in the eclipsing material with an inner scale of ~ 100 m and an outer scale of the size of the eclipse region can naturally explain the observation. Our results show that the eclipsing material in such systems can be highly turbulent and suggest that scattering is one of the main eclipsing mechanisms at around 1.4 GHz.

Key words: pulsars: general – pulsars: individual (PSR B1957+20)

1 INTRODUCTION

Eclipses of radio emission from pulsars are commonly observed in compact binary systems consisting of a millisecond pulsar (MSP) and a low-mass star ($< 1 M_{\odot}$). Such eclipses are generally believed to be caused by materials in the orbit interfering with the propagation of the radio emission and several eclipsing mechanisms have been proposed in the literature (see [Thompson et al. 1994](#), for a review). Thanks to extensive studies of a number of eclipsing pulsars, such as PSRs B1957+20 ([Fruchter et al. 1988b, 1990](#); [Polzin et al. 2020](#)), J1227-4853 ([Roy et al. 2015](#); [Kudale et al. 2020](#)), J1744+4937 ([Lyne et al. 1990](#)), J2051-0827 ([Stappers et al. 1998](#); [Polzin et al. 2019](#)), J1544+4937 ([Bhattacharyya et al. 2013](#)), PSR J1810+1744 ([Polzin et al. 2018](#)), our understanding of the eclipsing mechanism and properties of eclipsing materials have been greatly improved. Recently, [Kansabanik et al. \(2021\)](#) presented multi-frequency observations of PSR J1544+4937 and modelled its broadband radio spectrum. Their results suggested that synchrotron absorption by relativistic electrons is the dominating eclipsing mechanism at $\lesssim 1$ GHz.

As the first eclipsing pulsar discovered ([Fruchter et al. 1988a](#)), PSR B1957+20 and its companion have been studied in great detail at multiple wavelengths from radio (e.g., [Fruchter et al. 1990](#); [Polzin et al. 2020](#)) to optical (e.g., [Fruchter et al. 1988b](#); [Kulkarni & Hester 1988](#); [van Paradijs et al. 1988](#); [van Kerkwijk et al. 2011](#)) and

X-ray (e.g., [Stappers et al. 2003](#)). The detection of plasma lensing effect close to the eclipse makes PSR B1957+20 unique to probe not only eclipsing materials but also pulsar radiation mechanisms (e.g., [Main et al. 2017, 2018](#); [Mahajan et al. 2018](#); [Li et al. 2019](#)). Early observations with the Arecibo telescope showed that the eclipse duration is frequency (ν) dependent and roughly follows $\nu^{-0.41}$ ([Fruchter et al. 1990](#); [Ryba & Taylor 1991](#)). Before and after the eclipse, the pulsar signal is delayed by as much as 400 μs , which can be explained by an excess of ionized medium with a column density of free electrons of $\sim 10^{17} \text{ cm}^{-2}$ ([Fruchter et al. 1990](#); [Ryba & Taylor 1991](#)). Recently, [Polzin et al. \(2020\)](#) presented a study of PSR B1957+20 at low radio frequencies, and their measurements of eclipse duration and dispersion measure (DM) excess generally agree with previous results.

Based on early observations, [Thompson et al. \(1994\)](#) examined a range of eclipsing mechanisms for PSR B1957+20. They concluded that a favoured model is cyclotron or synchrotron absorption by plasma embedded in the pulsar wind combined with pulse smearing at high frequency (i.e. 1.4 GHz). However, the cyclotron absorption mechanism is challenged by tight upper limits on the strength of magnetic fields near the eclipse obtained through studies of plasma lensing ([Li et al. 2019](#)). [Polzin et al. \(2020\)](#) presented simultaneous measurements of pulsed and continuum flux densities of PSR B1957+20 at 150 MHz and showed that the pulsar signal is removed from the line of sight throughout the main body of the eclipse, which supports absorption or nonlinear scattering eclipse mechanisms. While [Polzin et al. \(2020\)](#) observed some evidence of

* E-mail: Shi.Dai@westernsydney.edu.au (SD)

† E-mail: qjzhi@gznu.edu.cn (QJZ)

pulse profile broadening at the edge of eclipse region, whether scattering is playing an important role is inconclusive. Previously, strong scattering has only been observed in PSR B1259–63 close to its eclipse and was suggested to originate from plasma density fluctuations in the disk of its companion Be star (Johnston et al. 1996). You et al. (2018) observed depolarisation of radio emission from PSR J1748–2446A at particular orbital phases and suggested that this depolarisation occurs because of rotation-measure fluctuations resulting from turbulence in the stellar wind.

While several eclipsing mechanisms, such as cyclotron/synchrotron absorption, pulse smearing, and scattering, are strong at low frequencies, it is challenging to distinguish them from each other at low frequencies. High signal-to-noise ratio (S/N) observations at high frequencies are therefore extremely valuable for us to get a wideband understanding of these mechanisms and compare them with theoretical predictions. Because of its steep spectrum (e.g., Fruchter et al. 1990), previous observations of PSR B1957+20 at high frequencies (e.g., 1.4 GHz) have limited sensitivities to probe various eclipsing mechanisms. In this paper we present multiple observations of the eclipse of PSR B1957+20 centred at ~ 1.25 GHz using the Five-hundred-meter Aperture Spherical Telescope (FAST, Nan et al. 2011; Li et al. 2018; Jiang et al. 2019). We present the first measurement of pulse scattering close to the eclipse and new measurements of the eclipsing duration and aim to shed new light on the eclipsing mechanism and properties of eclipsing materials. Details of observations and data processing are provided in Section 2. In Section 3, we present our measurements of the frequency dependence of the eclipse duration and pulse scattering. Section 4 gives discussions and conclusions.

2 OBSERVATIONS AND DATA PROCESSING

Three observations of PSR B1957+20 were taken using the central beam of the 19-beam receiver of FAST. Observations on 2019 August 8 (2.25 hr) and 2020 January 22 (3.5 hr) covered the whole eclipsing period while the observation on 2020 January 27 (2.4 hr) only covered a fraction of the eclipse and the egress. Data were recorded with the Reconfigurable Open Architecture Computing Hardware generation 2 (ROACH2)¹ backend in the pulsar search-mode with 8-bit sampling and 4096 channels within a frequency range from 1050 to 1450 MHz. Only the total intensity were recorded and therefore we do not have full polarisation information. A time resolution of either 98.304 or 49.152 μ s were used for these observations.

Search-mode data were folded with DSPSR (van Straten & Bailes 2011) using pulsar parameters obtained from the Australian Telescope National Facility Pulsar Catalog (PSRCAT V1.64²) (Manchester et al. 2005). Because of variations in orbital parameters often observed in eclipsing binary systems (e.g. Arzoumanian et al. 1994; Shaifullah et al. 2016), we observed significant pulse drifting in phase with these parameters, which reduces the S/N of detection. In order to maximize the S/N of folded profiles, we re-folded each epoch with a refined set of parameters. These refined parameters were determined, for each epoch, by measuring time of pulse arrivals (ToAs) away from the eclipse and refitting for the spin frequency and its derivative ($F0$ and $F1$), the orbital period (P_B) and the time of ascending node ($T0$) using TEMPO2 (Hobbs et al. 2006)³. Refolded observations have 1 s

sub-integration time, 256 pulse phase bins and 1024 frequency channels (corresponding to a frequency resolution of 488.3 kHz). Strong radio-frequency interference (RFI) were identified and masked using the PAZ and PAZI commands of PSRCHIVE⁴ (Hotan et al. 2004). Flux densities were measured using the PSRFLUX command of PSRCHIVE with a standard template (see e.g., Kumamoto et al. 2021, for details). A series of standard template was generated as a function of the orbital phase (every 5 minutes) in order to account for changes in the shape of pulse profile due to smearing and scattering.

To measure the DM as a function of the orbital phase, we further averaged the folded pulse profile to have a time resolution of 30 s and a frequency resolution of 50 MHz. As we go deeper into the eclipse region, the DM excess becomes large. In order to minimize the DM smearing, for each 30 s of data, we first used the PDMP command of PSRCHIVE to obtain a rough estimate of the DM and then re-folded the search-mode data with the updated DM. A standard template was generated using the re-folded pulse profile. ToAs were then measured for each channel and the DM was measured using TEMPO2.

The duration of eclipse was measured following the method described in Polzin et al. (2020) and Broderick et al. (2016). Measured flux densities were normalised so that the mean flux density of out-of-eclipse region was uniform. The eclipse ingress and egress flux densities, f , as a function of the orbital phase, ϕ , were fitted to a Fermi-Dirac type function, $f = [e^{\frac{\phi-p_1}{p_2}} + 1]^{-1}$, where p_1 is the orbital phase where the flux is half the out-of-eclipse value and p_2 is the slope. Flux densities were measured every 5 s using pulse profiles with updated DMs.

To search for evidence of pulse scattering and measure the scattering time-scale, we assumed that the observed pulse profile close to the eclipse region is the convolution of a standard template with a one-sided exponential decay function (e.g., Lewandowski et al. 2013),

$$s(t) = \exp\left(\frac{-t}{\tau_s}\right)H(t) \quad (1)$$

where τ_s is the pulse scattering time-scale and $H(t)$ is equal to zero for $t < 0$, and one otherwise. This assumes a thin scattering screen located in between the pulsar and the observer. The standard template was formed using a high S/N pulse profile away from the eclipse. We computed the convolution numerically and fitted for the pulse scattering time-scale using the BILBY⁵ package in python (Ashton et al. 2019). BILBY is a user-friendly Bayesian inference library to perform parameter estimation. The pulse scattering time-scale was measured for each 60 s window covering orbital phases from 0.22 to 0.29. We assumed a Gaussian-likelihood function with a uniform prior for each parameter. The uncertainty of τ_s was estimated as the average of deviations from the median at 16 per cent and 84 per cent of its posterior distribution.

3 RESULTS

3.1 Eclipse duration

Normalised flux densities measured on 2019 August 8 (top panel) and 2020 January 22 (bottom panel) are shown in Fig. 1 as a function of the orbital phase. While the light curve during the ingress is similar

our purpose of minimising pulse smearing due to the variation of orbital parameters.

⁴ <https://psrchive.sourceforge.net/>

⁵ <https://lscsoft.docs.ligo.org/bilby/>

¹ <https://casper.berkeley.edu/>

² <https://www.atnf.csiro.au/research/pulsar/psrcat/>

³ We note that these parameters can be highly co-variant since our integration time is much shorter than the orbital period. However, this will not affect

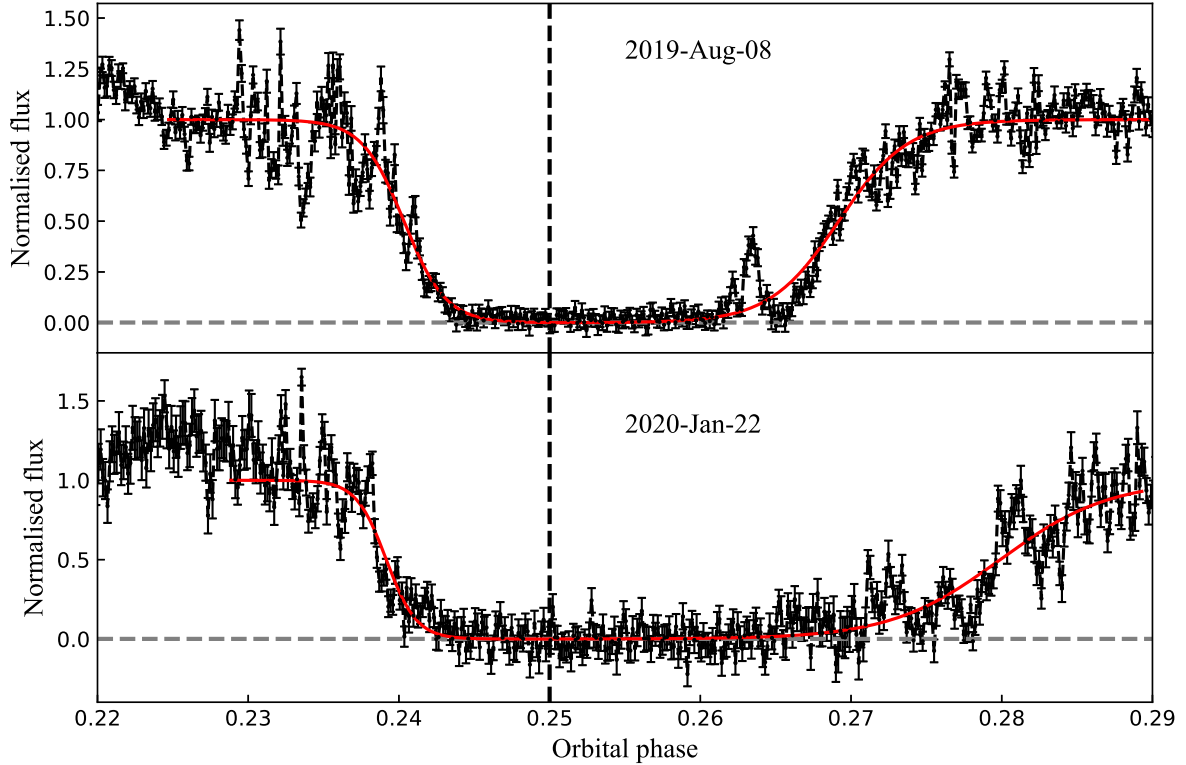


Figure 1. Normalized flux density of pulse emission as a function of orbital phase. Red lines show the least-squares fitting of a Fermi–Dirac function to the ingresses and egresses of eclipse.

for the two observations, it is significantly different during the egress, which has also been reported by previous observations (Fruchter et al. 1990; Ryba & Taylor 1991; Polzin et al. 2020). We detected a sudden increase of flux density at orbital phases from ~ 0.261 to 0.265 on 2019 August 8, which is well within the eclipse region that previous observations suggested and has not been observed before.

We measured the duration of eclipse as described in Section 2. The duration of eclipse ingress and egress ($\Delta\phi_{\text{in}}$ and $\Delta\phi_{\text{eg}}$) are defined as the orbital phase difference between ingress/egress and inferior conjunction of the companion, $\phi = 0.25$. The total eclipse ($\Delta\phi_{\text{eclipse}}$) is defined as the orbital phase difference between ingress and egress measured at 1250 MHz. Fig. 2 shows measured eclipse duration as a function of the observing frequency. For comparison, we also plotted recent low-frequency measurements from Polzin et al. (2020) (green points) and previous Arecibo measurements (grey and black points Ryba & Taylor 1991; Polzin et al. 2020).

3.2 Pulse scattering

The averaged pulse profile away from the eclipse region is shown in the top panel of Fig. 3 as a black solid line. In addition to a narrow main pulse and a broad, asymmetric interpulse (Fruchter et al. 1990), we detected a new shallow pulse component at the pulse phase ~ 0.6 . As we move deeper into the eclipse region, the pulse profile becomes significantly wider. As an example, in the top panel of Fig. 3, we show

the averaged pulse profile at the orbital phase 0.238 observed on 2019 August 8 as a blue dashed line. In the bottom panels of Fig. 3, we show the main pulse component at the same orbital phase but at four different observing frequencies. Strong evidence of pulse scattering can be observed at low frequencies, especially for the Gaussian-like main pulse component.

For each 60 s time window, we split our observing band into four sub-bands and fitted for the pulse scattering time-scale in each sub-band following the procedure described in Section 2. Taking pulse profiles at the orbital phase 0.238 as an example, in the bottom panels of Fig. 3, we show the best-fit exponential decay function as green dashed lines and the convolution of a Gaussian pulse (dashed black lines) and the exponential decay function as red solid lines. Residuals of the fitting are shown in the bottom as dashed black lines. In Table 1, we present scattering time-scale measurements as a function of the observing frequency at multiple orbital phases close to the eclipse. We also tried to measure the scattering index by fitting for a power-law, $\tau_s = \tau_0\nu^\alpha$, and present the index, α in the second last column of Table 1. In Table 1, we only presented scattering time-scales and scattering indices with uncertainty less than 20% of the measurement, which we consider reliable.

In Table 1 we also present measured DM excesses for these orbital phases. Similar to the flux density variation, we observed large variations of DM close to the egress of eclipse and show different trends in different observations while DMs close to the ingress show

Table 1. Measurements of the scattering time-scale (τ_s), the scattering index (α) and the DM excess (ΔDM).

| Date of obs. | Orbital phase | τ_s (μs) | | | | α | ΔDM ($pc\ cm^{-3}$) |
|--------------|---------------|----------------------|----------------------|-------------------|-----------------|----------------|----------------------------------|
| | | 1100 MHz | 1200 MHz | 1300 MHz | 1400 MHz | | |
| 2019-Aug-08 | | | | | | | |
| | 0.2326 | $19.5^{+0.4}_{-0.4}$ | $14.5^{+0.9}_{-0.8}$ | | | | 0.035 ± 0.001 |
| | 0.2344 | $15.5^{+0.3}_{-0.3}$ | $12.9^{+0.9}_{-0.8}$ | 8^{+2}_{-1} | 14^{+2}_{-2} | | 0.035 ± 0.001 |
| | 0.2362 | $40.5^{+0.6}_{-0.5}$ | $33.9^{+1.0}_{-0.8}$ | 31^{+2}_{-2} | 30^{+3}_{-3} | -1.6 ± 0.3 | 0.046 ± 0.002 |
| | 0.2381 | $45.8^{+0.5}_{-0.6}$ | 36^{+1}_{-1} | 32^{+1}_{-1} | 20^{+2}_{-3} | -2.6 ± 0.4 | 0.057 ± 0.003 |
| | 0.2399 | 84^{+2}_{-2} | 90^{+3}_{-3} | 68^{+4}_{-3} | 68^{+6}_{-7} | | 0.078 ± 0.003 |
| | 0.2417 | 160^{+7}_{-7} | 105^{+6}_{-6} | 136^{+8}_{-9} | | | 0.13 ± 0.01 |
| | 0.2617 | 138^{+5}_{-5} | 111^{+4}_{-4} | 94^{+8}_{-9} | | -2.4 ± 0.1 | 0.08 ± 0.01 |
| | 0.2635 | 153^{+4}_{-3} | 103^{+9}_{-9} | 104^{+9}_{-11} | | | 0.10 ± 0.04 |
| | 0.2653 | 184^{+14}_{-12} | 133^{+15}_{-18} | | | | 0.083 ± 0.007 |
| | 0.2671 | 77^{+1}_{-2} | 54^{+1}_{-2} | 72^{+3}_{-1} | 31^{+6}_{-6} | | 0.053 ± 0.006 |
| | 0.2690 | $29.4^{+0.3}_{-0.4}$ | $23.2^{+0.8}_{-0.9}$ | 21^{+1}_{-1} | | -2.3 ± 0.4 | 0.045 ± 0.004 |
| | 0.2708 | $21.9^{+0.3}_{-0.4}$ | $18.6^{+0.6}_{-0.6}$ | 15^{+1}_{-1} | | -2.2 ± 0.4 | 0.046 ± 0.006 |
| | 0.2726 | $18.0^{+0.3}_{-0.4}$ | $10.4^{+0.7}_{-0.7}$ | | | | 0.030 ± 0.002 |
| | 0.2744 | $9.0^{+0.3}_{-0.3}$ | $7.9^{+0.6}_{-0.6}$ | | | | 0.021 ± 0.001 |
| 2020-Jan-22 | | | | | | | |
| | 0.2344 | $28.0^{+0.9}_{-0.9}$ | 19^{+1}_{-1} | | | | 0.041 ± 0.002 |
| | 0.2362 | 38^{+1}_{-1} | 16^{+1}_{-1} | 27^{+2}_{-2} | | | 0.043 ± 0.002 |
| | 0.2381 | $24.3^{+0.9}_{-1.0}$ | $24.5^{+1.0}_{-0.9}$ | 14^{+3}_{-3} | | | 0.051 ± 0.006 |
| | 0.2399 | 167^{+16}_{-13} | 94^{+6}_{-7} | 89^{+4}_{-5} | | | 0.08 ± 0.01 |
| | 0.2417 | 230^{+26}_{-25} | 98^{+9}_{-10} | 88^{+14}_{-16} | | | 0.07 ± 0.02 |
| | 0.2752 | 203^{+12}_{-12} | | 192^{+17}_{-19} | 122^{+9}_{-9} | | 0.12 ± 0.02 |
| | 0.2770 | 186^{+9}_{-8} | 146^{+12}_{-16} | | 60^{+6}_{-6} | -4.6 ± 0.7 | 0.126 ± 0.008 |
| | 0.2788 | 67^{+1}_{-1} | 59^{+2}_{-2} | 54^{+4}_{-4} | 37^{+3}_{-3} | | 0.096 ± 0.004 |
| | 0.2807 | 63^{+1}_{-1} | 56^{+2}_{-2} | 25^{+2}_{-2} | 26^{+4}_{-4} | | 0.097 ± 0.004 |
| | 0.2825 | 69^{+2}_{-1} | 57^{+4}_{-4} | 31^{+1}_{-1} | 46^{+6}_{-6} | -4.5 ± 0.8 | 0.092 ± 0.004 |
| | 0.2843 | $37.3^{+0.5}_{-0.5}$ | 37^{+1}_{-1} | 27^{+2}_{-2} | | | 0.073 ± 0.003 |
| | 0.2861 | $17.7^{+0.3}_{-0.4}$ | | 12^{+3}_{-3} | | | 0.058 ± 0.002 |
| 2020-Jan-27 | | | | | | | |
| | 0.2734 | 74^{+3}_{-3} | 73^{+6}_{-6} | 51^{+3}_{-2} | | | 0.093 ± 0.006 |
| | 0.2752 | 76^{+3}_{-3} | 84^{+7}_{-6} | 51^{+4}_{-4} | | | 0.094 ± 0.008 |
| | 0.2770 | 142^{+9}_{-10} | 115^{+9}_{-10} | 104^{+5}_{-5} | | -1.8 ± 0.3 | 0.17 ± 0.04 |
| | 0.2861 | 124^{+5}_{-5} | 82^{+8}_{-8} | 66^{+3}_{-3} | | -3.8 ± 0.3 | 0.072 ± 0.003 |
| | 0.2879 | $33.6^{+0.7}_{-0.7}$ | 31^{+2}_{-2} | 28^{+2}_{-2} | | -1.1 ± 0.2 | 0.049 ± 0.002 |

significantly less variation. We observed a maximum DM excess of $\sim 0.17\ pc\ cm^{-3}$ at the orbital phase 0.277 on 2020 January 27, which corresponds to an electron column density of $\sim 5.2 \times 10^{17}\ cm^{-3}$ in the eclipse region ($R_E \approx 10^8\ m$). This is consistent with the mean column density of electrons in the outer parts of the eclipsing medium measured by Ryba & Taylor (1991).

4 DISCUSSIONS AND CONCLUSIONS

In this paper, we presented highly sensitive observations of PSR B1957+20 centred at 1250 MHz using FAST. These observations allow us to probe much deeper into the eclipse region of PSR B1957+20 than previous observations. For the first time, we detected pulse scattering and measured scattering time-scales close to the eclipse region. We show that the measured scattering time-scale increases as we go deeper into the eclipse region and reaches a maximum of $\sim 0.2\ ms$ at $\sim 1.1\ GHz$.

The observed pulse broadening can be well described by the convolution of the intrinsic pulse profile and a one-sided exponential decay. We also observed that the scattering time-scale scales with the DM excess roughly as $\tau \propto \Delta DM^2$. These strongly suggest that scattering

is caused by multi-path propagation effects as radio waves traverse a turbulent plasma (e.g., Rickett 1990). However, the electron density in the scattering region must be $n_e \sim \Delta DM/R_E \approx 5 \times 10^7\ cm^{-3}$, where $R_E \approx 10^8\ m$ is the size of the eclipse region. This is comparable with the scattering in the solar corona (e.g., You et al. 2012) and at least seven orders of magnitude larger than normal interstellar scattering, so scattering angles and spatial scales will be quite different from normal pulsar observations.

Forward angular scattering due to a medium with variable refractive index is a second moment of the electric field and can be fully characterised by the phase structure function (see Coles et al. 1987, and reference therein). Our measurements of both scattering and electron density provide us the opportunity to investigate the property of eclipsing materials through analysis of the structure function. The angular spectrum of plane waves is $\Phi(\vec{k})$ where $\vec{k} = k\hat{\theta}$, $k = 2\pi/\lambda$ is the wave number and $\hat{\theta}$ is the scattering angle. It is the Fourier transform of the auto-correlation function $\rho_e(\vec{s})$. The latter is given exactly by $\rho_e(\vec{s}) = \exp(-0.5D_\phi(\vec{s}))$. Here $D_\phi(\vec{s}) = \langle (\phi(\vec{r}) - \phi(\vec{r} + \vec{s}))^2 \rangle$ is the phase structure function. If the medium is of limited extent, $\phi(\vec{r})$ has an auto-covariance $C_\phi(\vec{s}) = \langle \phi(\vec{r})\phi(\vec{r} + \vec{s}) \rangle$ and it is related to the

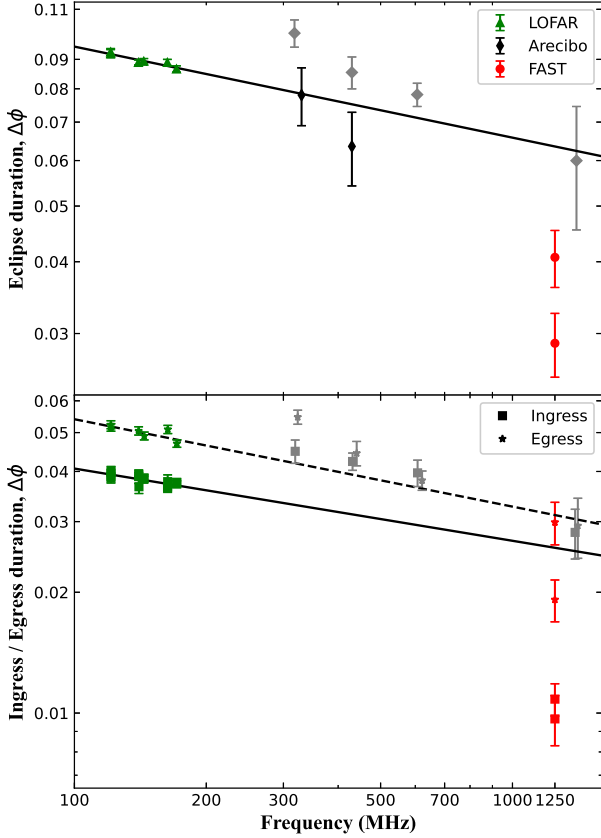


Figure 2. Top: total eclipse duration as a function of the observing frequency. Green, black and gray points are published measurements from Polzin et al. (2020) and Ryba & Taylor (1991). Red points are measurements using FAST observations on 2019 August 8 and 2020 January 22. Bottom: Ingress and egress duration as a function of the observing frequency. Colours are consistent with the top panel. In both panels, solid and dashed lines show the best-fit power-law model from Polzin et al. (2020).

structure function by

$$D_\phi(s) = 2[C_\phi(0) - C_\phi(\vec{s})]. \quad (2)$$

The angular spectrum is approximately Gaussian in shape, so the auto-correlation of the electric field is also approximately Gaussian. Thus we define the width of the auto-correlation as s_0 and the width of the spatial spectrum as $\kappa_0 = 1/s_0$, so $\theta_0 = 1/\kappa_0$ is the width of the angular spectrum. By definition then, $D_\phi(s_0) = 1$.

If the scattering medium is turbulent, the phase structure function will have the form $D_\phi(\vec{s}) \sim s^{5/3}$ in the magneto-hydrodynamic range, where $s_{\text{in}} < s < s_{\text{out}}$. In a hydrogen plasma, $s_{\text{in}} = 6.84 \times 10^5/n_e^{0.5}$ is the ion inertial scale in m, where n_e is in cm^{-3} (Coles & Harmon 1989). This gives an inner scale of $s_{\text{in}} \approx 100$ m for $n_e \approx 5 \times 10^7 \text{ cm}^{-3}$. In general, s_{out} is the extent over which the medium is homogeneous and we expect s_{out} to be of the order of $R_E \approx 10^8$ m in our case. For $s < s_{\text{in}}$, $D_\phi(s) \sim s^2$ and for $s > s_{\text{out}}$, $D_\phi(s) = D_\phi(s_{\text{out}})$.

We can measure s_0 using the observed scattering time scale τ_s , which is related to θ_0 as $a\theta_0^2/2c$. Here a is the distance from the pulsar to the scattering screen ($\sim 10^{11}$ cm). For $\tau_s = 0.2$ ms, we measured $s_0 = 4$ m, which is smaller than the inner scale and smaller by five orders of magnitude than typical ISM values (e.g., Keith et al. 2013). At much larger scales, $D_\phi(R_E)$ can be estimated from the observed ΔDM because ϕ and DM are both measures of the electron column density, so $\phi = A \times \text{DM}$ where, $A = 2\pi\nu \cdot [4.15 \text{ ms} \cdot (\frac{\nu}{1.1 \text{ GHz}})^{-2}] = 2.3701 \times 10^7$. We assume that the fluctuations in DM are roughly exponentially distributed so $\text{Variance}(\text{DM}) = \text{Mean}(\text{DM})^2$, and $D_{\text{DM}}(R_E) = 2\Delta\text{DM}^2 = 0.0512$.

Now we compare $D_{\text{DM}}(s)$ of the turbulent plasma model as described above with our observations. The most reliable measurement is s_0 , so we adjust our model so that $D_{\text{DM}}(s_0) = A^{-2}$. The resulting piece-wise linear $D_{\text{DM}}(s)$ is plotted as a red line on Fig. 4. We find that our estimate of $D_{\text{DM}}(R_E)$, shown as the red circle on Fig. 4, is a factor of five higher than the model. However, since large variations in both τ_s and ΔDM were measured (Table 1), the assumed density has enough uncertainty to match the model value of $D_{\text{DM}}(R_E)$. For example, it can be brought into agreement if we reduce the assumed root-mean-square (RMS) DM by a factor of ~ 2 .

The electron density fluctuations causing the angular scattering need not to be turbulent. They could have a single spatial scale s_{ne} , which can be modeled with a 3D Gaussian auto-covariance for n_e . The 2D auto-covariance of DM can be obtained by doing the line of sight integrals to obtain DM from n_e . The 2D structure function can then be obtained from Equation 2,

$$D_{\text{DM}}(s) = 2\text{Variance}(\text{DM})(1 - \exp(-0.5(s/s_{\text{ne}})^2)). \quad (3)$$

When $s_{\text{ne}} = R_E$, the line of sight integration is degenerate and $\text{Variance}(\text{DM}) = \delta n_e^2 R_E^2$. When $s_{\text{ne}} \ll R_E$, the line of sight integration gives $\text{Variance}(\text{DM}) = \sqrt{2\pi} \delta n_e^2 R_E s_{\text{ne}}$.

First we model the large scale fluctuations in DM as Gaussian, setting $s_{\text{ne}} = R_E$ and $\delta n_e = n_e$. This $D_{\text{DM}}(s)$ is plotted on Fig. 4 as a black line. One can see that it fails to provide enough scattering as the predicted structure function is lower by nearly two orders of magnitude at s_0 . In order to explain the observed angular scattering with this model, one needs to reduce s_{ne} by a factor of ~ 20 , which is shown with a cyan line in Fig. 4. Although technically possible, we should have observed such rapid and large variations in ΔDM close to the eclipse, so it seems unlikely.

Thompson et al. (1994) have suggested that strong scattering can be caused by Langmuir turbulence with the electron density fluctuations at extremely short scales. They noted that such short-scale plasma fluctuation need to be continuously regenerated and a promising source of energy is the relativistic particles from the pulsar wind. We have modeled this suggestion as a Gaussian process with a scale of s_0 . It would require an RMS electron density of $\delta n_e \sim 4.3 \times 10^4 \text{ cm}^{-3}$ to create the observed angular scattering. This structure function is shown as a blue line on Fig. 4, which fails to explain large scale fluctuations in DM. If the scattering medium had two static Gaussian components, one of scale R_E and another of scale s_0 , we would not be able to distinguish that from a single turbulent process. On the balance, we prefer the turbulent model as it fits the observations with minimal assumptions.

With measurements of the scattering time-scale at multiple frequencies, we tried to fit for a power-law, $\tau_s = \tau_0\nu^\alpha$, and measure the scattering index α . Because of the steep spectrum of PSR B1957+20, scattering time-scale measurements at high frequency subbands are poor with large uncertainties. Therefore, α is not well constrained. However, for those with relatively small uncertainties, we find that α varies from ~ -1.5 to -4.6 . Although an exponent of -4.4 is

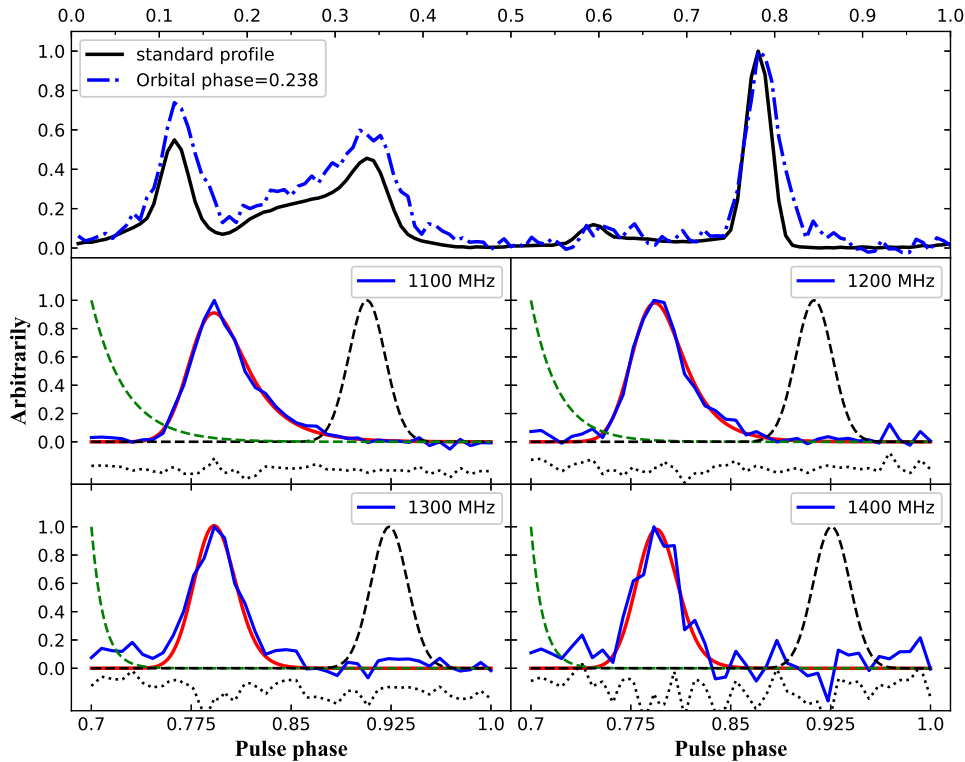


Figure 3. Top panel: the averaged pulse profile away from the eclipse region is shown as black solid line and the averaged pulse profile at orbital phase 0.238 is shown as blue dot dashed line. Bottom panels: The main pulse component at orbital phase 0.238 in four subbands (blue lines). Green lines show the best-fit exponential decay function. Red lines show the convolution of the best-fit exponential decay function with a template of the main pulse component (black dashed lines, Gaussian-like function). Black dotted lines show the residuals of fitting.

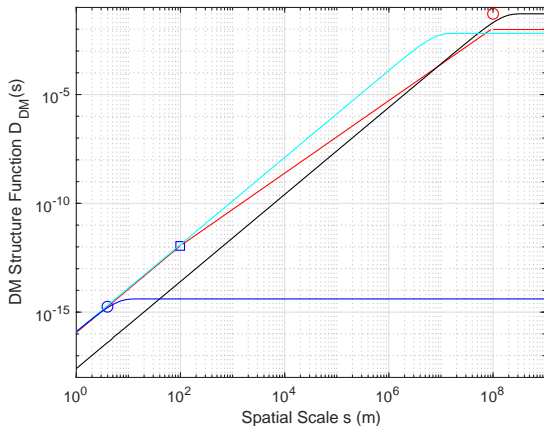


Figure 4. Structure function of DM as function of the spatial scale. The red piece-wise linear line represents a Kolmogorov process that matches the observations at s_0 , s_{in} and $s_{out} = R_e$. The black line represents a process with a Gaussian spatial scale of R_e and an RMS electron density $\delta n_e = n_e$. The cyan line represents a process with a Gaussian scale of $R_e/20$ and $\delta n_e = n_e$. The blue line represents a process with a Gaussian scale of s_0 and $\delta n_e = 4.3 \times 10^4 \text{ cm}^{-3}$. The blue circle and square show the measured coherent scale and estimated inner scale, respectively. The red circle shows the estimated $D_{DM}(R_e)$ based on ΔDM .

predicted for a scattering screen with Kolmogorov turbulence (e.g., Lee & Jokipii 1976; Rickett 1977), it would not be expected in our observations because the structure function is quadratic in the vicinity of s_0 . Thus the expected exponent is -4.0 regardless of whether it comes from a Gaussian process or a turbulent process which has become heavily damped by the scale of s_0 .

Our highly sensitive observations enable us to probe deeper into the eclipse region. The total eclipse duration is measured to be 0.029 ± 0.003 (16 ± 2 minutes) and 0.041 ± 0.004 (22 ± 3 minutes) at 1250 MHz on 2019-Aug-08 and 2020-Jan-22, respectively. This is significantly shorter than the previous Arecibo measurement of 0.06 ± 0.01 (33 ± 8 minutes) at 1400 MHz (Ryba & Taylor 1991). Both DM and flux density at the egress are highly variable, and we observed a sudden rise of flux density at the orbital phase of 0.263, deep into the eclipse region. This, again, shows that the trailing tail of eclipsing materials is highly clumpy (Tavani & Brookshaw 1991). While the egress duration is uncertain due to large flux density variations, we show that the ingress duration is much shorter than previously measured. Combining our measurements with previous low frequency measurements, we find that a single power-law cannot fit the frequency dependence of eclipse duration and the duration at 1.25 GHz is significantly shorter than previously expected.

Currently, the eclipsing mechanism and properties of eclipsing materials are still not well understood. Kudale et al. (2020) discussed several eclipse mechanisms for the case of PSR J1227-4853

and concluded that the eclipse was likely to be caused by cyclotron-synchrotron absorption. Kansabanik et al. (2021) modeled the broadband radio spectrum of PSR J1544+4937 at its full eclipse phase and showed that synchrotron absorption by relativistic electrons is favoured. In the case of PSR B1957+20, based on early observations Thompson et al. (1994) suggested that a favoured model is cyclotron or synchrotron absorption by plasma embedded in the pulsar wind combined with pulse smearing at high frequency (i.e., 1.4 GHz). More recently, low frequency observations carried out by Polzin et al. (2020) supported absorption or nonlinear scattering eclipse mechanisms. Our observations provided the first evidence of strong scattering close to the eclipse of PSR B1957+20 and confirmed that strong scattering is playing an important role at around 1.4 GHz. However, we show that even after considering the scattering the averaged flux density decreases as we go deeper into the eclipse, which suggests that other eclipsing mechanisms are also involved. Simultaneous measurements of pulsed and continuum flux densities of PSR B1957+20 close to the eclipse at around 1.4 GHz will help us better understand the contribution of pulse scattering.

Neutron stars in binary systems or other extreme environment have been suggested to be possible origins of fast radio bursts (FRBs, e.g., Zhang 2017; Margalit & Metzger 2018; Lyutikov et al. 2020). In these models radio emission from neutron stars are expected to propagate through their surrounding dense and ionised medium, which is similar to the case of eclipsing binaries. Observationally, strong pulse scattering have been observed in both non-repeating (e.g., Osłowski et al. 2019; Qiu et al. 2020) and repeating FRBs (Niu et al. 2021). There are also increasing evidence of dense ionised medium surrounding FRB sources, especially those active repeating ones (e.g., Michilli et al. 2018; Feng et al. 2022; Anna-Thomas et al. 2022; Dai et al. 2022). Studies of the scattering of FRB 190520B implied distance between the FRB source and dominant scattering material is $\lesssim 100$ pc (Ocker et al. 2022). Our detection of strong scattering close to the eclipse of PSR B1957+20 show that ionised medium surrounding neutron stars in eclipsing binary systems can be highly turbulent and responsible for the observed scattering. Future observation of pulse scattering of FRBs may provide additional information about their origin.

ACKNOWLEDGMENTS

We thank Stefan Osłowski and Congyao Zhang for useful discussions. This work made use of the data from FAST (Five-hundred-meter Aperture Spherical radio Telescope). FAST is a Chinese national mega-science facility, operated by National Astronomical Observatories, Chinese Academy of Sciences. SD is the recipient of an Australian Research Council Discovery Early Career Award (DE210101738) funded by the Australian Government. This work was funded by the National Natural Science Foundation of China (Nos.U1731238, 11565010), Foundation of Science and Technology of Guizhou Province Nos. (2016)4008, (2017)5726-37 and Foundation of Guizhou Provincial Education Department (No. KY(2020)003). This work is supported by the National Natural Science Foundation of China under Grand No. 11703047, 11773041, U2031119, and 12173052. ZP is supported by the CAS “Light of West China” Program. Shijun Dang is supported by Guizhou Provincial Science and Technology Foundation (Nos. ZK[2022]304)

DATA AVAILABILITY

The observations from the FAST radio telescope are publicly available from <https://fast.bao.ac.cn/> after an 12 month embargo period. Note that all original data used in this paper are out of this embargo period and are available upon request. Processed data products used in this paper are available from <https://www.scidb.cn/en/doi/10.11922/sciencedb.01629>.

REFERENCES

- Anna-Thomas R., et al., 2022, arXiv e-prints, p. arXiv:2202.11112
 Arzoumanian Z., Fruchter A. S., Taylor J. H., 1994, *ApJ*, 426, L85
 Ashton G., et al., 2019, *ApJS*, 241, 27
 Bhattacharyya B., et al., 2013, *ApJ*, 773, L12
 Broderick J. W., et al., 2016, *MNRAS*, 459, 2681
 Coles W. A., Harmon J. K., 1989, *ApJ*, 337, 1023
 Coles W. A., Frehlich R. G., Rickett B. J., Codona J. L., 1987, *ApJ*, 315, 666
 Dai S., et al., 2022, arXiv e-prints, p. arXiv:2203.08151
 Feng Y., et al., 2022, arXiv e-prints, p. arXiv:2202.09601
 Fruchter A. S., Stinebring D. R., Taylor J. H., 1988a, *Nature*, 333, 237
 Fruchter A. S., Gunn J. E., Lauer T. R., Dressler A., 1988b, *Nature*, 334, 686
 Fruchter A. S., et al., 1990, *ApJ*, 351, 642
 Hobbs G. B., Edwards R. T., Manchester R. N., 2006, *MNRAS*, 369, 655
 Hotan A. W., van Straten W., Manchester R. N., 2004, *Publ. Astron. Soc. Australia*, 21, 302
 Jiang P., Peng B., Li D., Xu R., 2019, arXiv e-prints, p. arXiv:1903.07240
 Johnston S., Manchester R. N., Lyne A. G., D’Amico N., Bailes M., Gaensler B. M., Nicastro L., 1996, *MNRAS*, 279, 1026
 Kansabanik D., Bhattacharyya B., Roy J., Stappers B., 2021, *ApJ*, 920, 58
 Keith M. J., et al., 2013, *MNRAS*, 429, 2161
 Kudale S., Roy J., Bhattacharyya B., Stappers B., Chengalur J., 2020, *ApJ*, 900, 194
 Kulkarni S. R., Hester J. J., 1988, *Nature*, 335, 801
 Kumamoto H., et al., 2021, *MNRAS*, 501, 4490
 Lee L. C., Jorjipii J. R., 1976, *ApJ*, 206, 735
 Lewandowski W., Dembska M., Kijak J., Kowalińska M., 2013, *MNRAS*, 434, 69
 Li D., et al., 2018, *IEEE Microwave Magazine*, 19, 112
 Li D., Lin F. X., Main R., Pen U.-L., van Kerkwijk M. H., Yang I. S., 2019, *MNRAS*, 484, 5723
 Lyne A. G., et al., 1990, *Nature*, 347, 650
 Lyutikov M., Barkov M. V., Giannios D., 2020, *ApJ*, 893, L39
 Mahajan N., van Kerkwijk M. H., Main R., Pen U.-L., 2018, *ApJ*, 867, L2
 Main R., van Kerkwijk M., Pen U.-L., Mahajan N., Vanderlinde K., 2017, *ApJ*, 840, L15
 Main R., et al., 2018, *Nature*, 557, 522
 Manchester R. N., Hobbs G. B., Teoh A., Hobbs M., 2005, *AJ*, 129, 1993
 Margalit B., Metzger B. D., 2018, *ApJ*, 868, L4
 Michilli D., et al., 2018, *Nature*, 553, 182
 Nan R., et al., 2011, *International Journal of Modern Physics D*, 20, 989
 Niu C. H., et al., 2021, arXiv e-prints, p. arXiv:2110.07418
 Ocker S. K., et al., 2022, arXiv e-prints, p. arXiv:2202.13458
 Osłowski S., et al., 2019, *MNRAS*, 488, 868
 Polzin E. J., et al., 2018, *MNRAS*, 476, 1968
 Polzin E. J., Breton R. P., Stappers B. W., Bhattacharyya B., Janssen G. H., Osłowski S., Roberts M. S. E., Sobey C., 2019, *MNRAS*, 490, 889
 Polzin E. J., Breton R. P., Bhattacharyya B., Scholte D., Sobey C., Stappers B. W., 2020, *MNRAS*, 494, 2948
 Qiu H., et al., 2020, *MNRAS*, 497, 1382
 Rickett B. J., 1977, *ARA&A*, 15, 479
 Rickett B. J., 1990, *ARA&A*, 28, 561
 Roy J., et al., 2015, *ApJ*, 800, L12
 Ryba M. F., Taylor J. H., 1991, *ApJ*, 380, 557
 Shaifullah G., et al., 2016, *MNRAS*, 462, 1029
 Stappers B. W., Bailes M., Manchester R. N., Sandhu J. S., Toscano M., 1998, *ApJ*, 499, L183

- Stappers B. W., Gaensler B. M., Kaspi V. M., van der Klis M., Lewin W. H. G., 2003, *Science*, 299, 1372
- Tavani M., Brookshaw L., 1991, *ApJ*, 381, L21
- Thompson C., Blandford R. D., Evans C. R., Phinney E. S., 1994, *ApJ*, 422, 304
- You X. P., Coles W. A., Hobbs G. B., Manchester R. N., 2012, *MNRAS*, 422, 1160
- You X. P., Manchester R. N., Coles W. A., Hobbs G. B., Shannon R., 2018, *ApJ*, 867, 22
- Zhang B., 2017, *ApJ*, 836, L32
- van Kerkwijk M. H., Breton R. P., Kulkarni S. R., 2011, *ApJ*, 728, 95
- van Paradijs J., et al., 1988, *Nature*, 334, 684
- van Straten W., Bailes M., 2011, *Publ. Astron. Soc. Australia*, 28, 1

This paper has been typeset from a $\text{\TeX}/\text{\LaTeX}$ file prepared by the author.